# Photochemical Microscale Electrophoresis Allows Fast Quantification of Biomolecule Binding

Friederike M. Möller, Michael Kieß, and Dieter Braun*

Systems Biophysics, Physics Department, Nanosystems Initiative Munich and Center for NanoScience, Ludwig-Maximilians-Universität München, Amalienstraße 54, 80799 München, Germany

Ⓢ *Supporting Information*

ABSTRACT: Intricate spatiotemporal patterns emerge when chemical reactions couple to physical transport. We induce electrophoretic transport by a confined photochemical reaction and use it to infer the binding strength of a second, biomolecular binding reaction under physiological conditions. To this end, we use the photoactive compound 2-nitrobenzaldehyde, which releases a proton upon 375 nm irradiation. The charged photoproducts locally perturb electroneutrality due to differential diffusion, giving rise to an electric potential Φ in the 100 μV range on the micrometer scale. Electrophoresis of biomolecules in this field is counterbalanced by back-diffusion within seconds. The biomolecule concentration is measured by fluorescence and settles proportionally to $\exp(-\mu/D\,\Phi)$. Typically, binding alters either the diffusion coefficient D or the electrophoretic mobility μ. Hence, the local biomolecule fluorescence directly reflects the binding state. A fit to the law of mass action reveals the dissociation constant of the binding reaction. We apply this approach to quantify the binding of the aptamer TBA15 to its protein target human-α-thrombin and to probe the hybridization of DNA. Dissociation constants in the nanomolar regime were determined and match both results in literature and in control experiments using microscale thermophoresis. As our approach is all-optical, isothermal and requires only nanoliter volumes at nanomolar concentrations, it will allow for the fast screening of biomolecule binding in low volume multiwell formats.
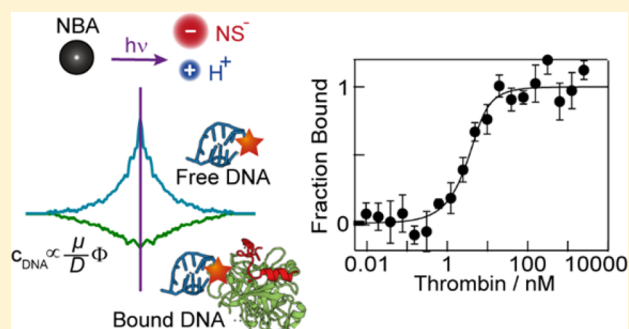
INTRODUCTION

Driving reactions out of equilibrium is a standard method for analytical measurements in chemistry. The perturbations are most often macroscopic in scale and are imposed externally. For example, electric fields are applied by electrodes in mass spectrometry and gel electrophoresis. In nuclear magnetic resonance (NMR) techniques, electromagnetic fields are absorbed and re-emitted by nuclei to be detected by coils inside magnetic fields. Here, we scale down free solution electrophoresis to the nano- to microscale. We show that the electric field for the separation of biomolecule species can be generated by chemistry itself without external electrodes. A localized light field supplies the energy to build up the electric field.

We apply photochemically triggered microscale electrophoresis (PME) as a tool for the quantification of biomolecular interactions. Binding events between proteins, DNA, and small molecules and their quantification are essential for the investigation of cellular and molecular mechanisms in biology, in biotechnological applications and, perhaps most importantly, in drug development.

A typical application is the development of new aptamers. These small single-stranded DNAs (ssDNA) bind specifically to target molecules, such as ions, proteins, or whole cells. Since their introduction in 1990,[1] they have been widely employed in biotechnology,[2] diagnostics,[3] and therapeutics.[4]

In the past decade, several biophysical approaches emerged for the quantification of binding interactions in free solution relying on binding induced changes in size[5] (dynamic light scattering), heat flux[6] (isothermal titration calorimetry), refractive index[7] (back scattering interferometry), or Soret coefficient[8] (microscale thermophoresis). Electrophoresis-based biochemical approaches, such as electrophoretic mobility shift assays (EMSA) and enzyme-linked immunosorbent assays (ELISA), have already been applied for decades. However, such approaches rather provide semiquantitative results and cannot be conducted in free solution or physiological buffers.[9] Capillary electrophoresis (CE) enabled quantitative free solution binding analysis with electrophoretic mobility as discrimination parameter.[10,11] Advances in microfluidic approaches reduce sample volumes and allow a higher electric field, which speeds up separation and increases resolution.[12] However, it has been shown that high electric field strengths destabilize protein−DNA interactions.[13] Joule heating and electroosmotic flows can further obstruct experiments.[14,15] But most importantly, the sensitivity of gel-free electrophoretic

separation is limited. For example, highly charged, free draining polymers, such as double-stranded DNA (dsDNA) of different length cannot be separated by electrophoresis in free solution, but only by using drag tags[16] or sieving matrices.[17]

In contrast to the described electrophoresis-based methods, binding quantification with PME not only relies on changes in electrophoretic mobility but is in addition size selective. The reason is that the photochemically induced electric field only spans over tens of micrometers. On this scale, transport is diffusion limited, and the steady state is determined by both diffusion coefficient D and electrophoretic mobility μ, which enhances the sensitivity to detect binding even in free solution. As a result, we succeed in determining dissociation constants in the nanomolar regime for the well-characterized thrombin-binding aptamer TBA15[18−20] and DNA hybridization.

In this work, we exploit PME as a tool for binding quantification. However, it should be noted that in developing PME we follow strategies of living systems, which abundantly couple chemical reactions and physical transport phenomena. We thus borrow and explore the biotechnology that cellular life invented in the course of evolution, following the bottom up approach of synthetic biology.[21−23]

Reaction−diffusion systems are ubiquitous in living systems. They are found in morphogenesis, animal markings, and cellular signaling pathways. In a simplified picture, photosynthesis also represents a light-driven reaction-transport system. A light-dependent reaction creates a proton gradient. The induced nonequilibrium generates directed transport of protons and drives another chemical reaction, namely ATP synthesis.

In various fields of science, researchers mimic such complex systems from scratch in the laboratory. For this purpose, laser beams are a convenient energy source due to their high spatial and temporal resolution. For example, it has been shown that patterned illumination of photoactive compounds can control nanomachines[24] and mimic energy fluxes in a simple protometabolism.[25] In a different approach, a light-sensitive chemical reaction network has been exploited to perform pattern transformation tasks, such as edge detection.[26]

With PME, we extend such photochemical reaction-diffusion systems toward a reaction-diffusion-migration system. We show that localized photochemistry can not only generate steep concentration gradients but also induce charge separation. The resulting electric field transports biomolecules, such as DNA, by electrophoresis. In contrast to standard free solution electrophoresis, the electric field only spans the micrometer scale, and transport is diffusion-limited. In this way, we use a light-driven chemical reaction to induce physical transport, which can quantify a second chemical reaction.

■ RESULTS

Photochemical Electric Field Generation and Electrophoretic Transport. In our experiments, we move biomolecules by electrophoresis. The driving electric field is generated by the spatially confined light-triggered dissociation of 2-nitrobenzaldehyde (NBA) into a 2-nitrosobenzoic anion (NS$^-$) and a proton (H$^+$) (Figure 1a). The localized reaction leads to a steep concentration gradient of differently charged photoproducts. Due to the considerably different diffusion coefficients D_{H^+} and D_{NS^-}, a net charge distribution emerges which generates an electric field on the microscale. As a result, charged macromolecules, such as DNA or proteins, move outward by electrophoresis (Figure 1b).
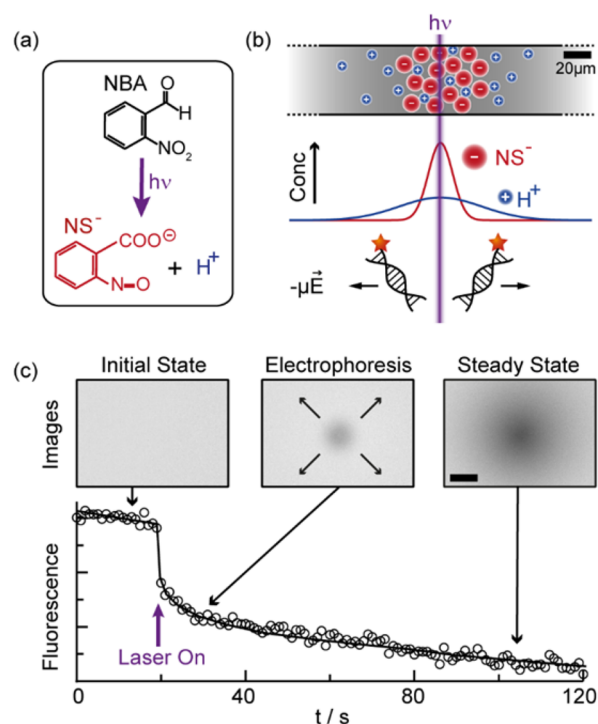

Figure 1. Generation of a microscale electric field by phototriggered dissociation of NBA and directed transport of biomolecules. (a) Photochemical dissociation of NBA. (b) Focused 375 nm irradiation (HWHM = 3 μm) of the sample solution within a capillary with a cross-section of 50 × 500 μm^2. The difference in diffusion speed of the differently charged photoproducts leads to a radial net charge distribution on the micrometer scale. This electric field transports negatively charged biomolecules, such as DNA, out of the laser focus. (c) Fluorescence images of labeled ssDNA over time. The depletion of fluorescence upon laser irradiation reflects the electrophoresis, directed outward from the laser focus. Photobleaching is the cause of the superposed fluorescence decrease throughout the experiment.

We observe the directed accumulation or depletion of the biomolecules by epifluorescence inside a glass capillary (0.05 × 0.5 × 50 mm^3). The sample volume for each measurement is around 1 μL, but the observation volume for a single experiment is only about 2 nL. Photolysis is achieved by a 375 nm laser, which is focused mildly to the center of the capillary by a lens with an effective numerical aperture (NA) of 0.1. We measure a half width at half-maximum intensity of 3 μm. To avoid crosstalk, a chopper wheel is synchronized to the camera, and images are taken while the laser light is blocked. A detailed sketch of the optical setup and the beam path is provided in the Supporting Information.

Figure 1c shows a typical fluorescence time trace at the laser spot position and the corresponding fluorescence images. In the initial state before the laser is switched on, a homogeneous fluorescence intensity F_0 is observed. Upon laser irradiation, two processes on different time scales set in. A steep drop in fluorescence is observed within ∼1 s after the laser is switched on. This agrees with the expected time scale for the equilibration of the electric field, which is determined by the characteristic diffusion times $t_i = (50\ \mu m)^2 / D_i \approx 0.2−3$ s of the ionic species i in solution. For this estimation, we approximate the characteristic length scale of the electric field as 50 μm (Figure 2c) and the diffusion coefficients of the photoproducts as $D_{H^+} \approx 9000\ \mu m^2/s$ and $D_{NS^-} \approx 800\ \mu m^2/s$. Further contributions to the steep fluorescence drop stem from laser-
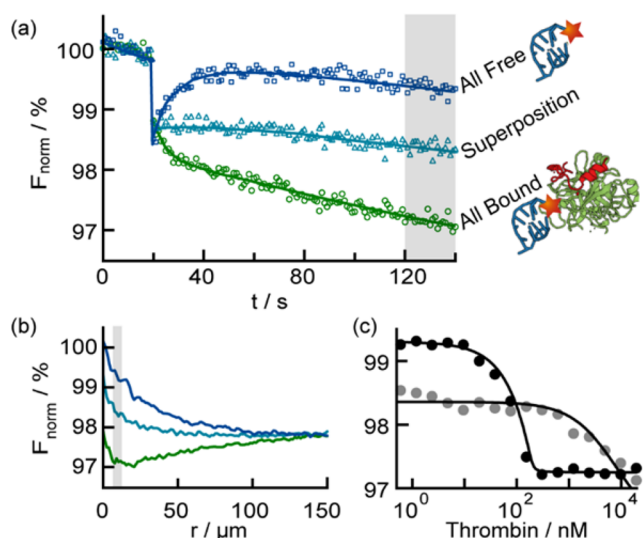
Figure 2. Biomolecule depletion or accumulation indicates aptamer binding reaction. (a) Normalized fluorescence F_{norm} over time for the aptamer at three different thrombin concentrations (blue, 1.19 nM; turquoise, 152 nM; green, 9.75 μM), showing the depletion contrast upon binding. The rapid drop in fluorescence can be attributed to fast processes during electric field stabilization, laser-induced bleaching, and the pH dependence of the dye, as the pH is decreased by the photoreaction. (b) Radial fluorescence distributions after 110 s of local photolysis. (c) F_{norm} at different thrombin concentrations for the TBA15 aptamer (black) and its dinucleotide mutant (gray) both at a concentration of 200 nM. F_{norm} is evaluated and averaged over a time interval of 25 s in steady state and within a radial area between $r = 5$ μm and $r = 10$ μm from the laser spot, as indicated by the gray shaded regions in panels (a) and (b). The fluorescence follows the probability of bound complex calculated from the mass action law of the binding reaction.

induced bleaching and the pH dependence of the dye, as the pH is decreased by the photoreaction. After equilibration of the field, the normalized fluorescence $F_{norm} = F/F_0$ mainly reflects the concentration change of the labeled biomolecules, e.g., DNA, due to electrophoretic transport. This active transport process is counterbalanced by passive back-diffusion, and the steady state is reached within tens of seconds ($t_{DNA} = (50 \ \mu m)^2/D_{DNA} \approx 15$ s with $D_{DNA} \approx 160 \ \mu m^2/s$). The radial steady-state concentration distribution $c(r)$ with r being the distance from the laser spot is described by

$$c(r) = c_0 \exp\left(-\frac{\mu}{D}\phi(r)\right) \approx c_0\left(1 - \frac{\mu}{D}\phi(r)\right) \qquad (1)$$

where D and μ are the diffusion coefficient and the electrophoretic mobility of the labeled biomolecule and $\phi(r)$ the induced electric potential at radius r. A derivation from the flux equations is presented in the Supporting Information.

In the simplest case without any buffer reactions, a negative charge surplus at the laser position emerges. As a consequence, the local concentration of negatively charged macromolecules, such as DNA, depletes around the laser position until electrophoresis and diffusion balance out. The presence of buffers makes the situation less intuitive, as concentration distributions of all buffer components need to be considered for net charge density calculations. This renders the induced electric potential highly dependent on the buffer reaction equilibria, as well as on the mobilities and diffusion coefficients of all buffer components. However, the buffer is not changed

significantly under titration experiments for binding quantification. Hence, even potentially complex buffer conditions and with them the resulting electric field are to a good approximation constant for a binding analysis.

In total, the normalized fluorescence in the steady state upon local photolysis can be described by

$$F_{norm} = 1 - \frac{\mu}{D}\phi + \frac{\partial F}{\partial \text{pH}}\Delta \text{pH} \qquad (2)$$

The ratio μ/D depends on a molecule's size, charge, and ionic environment and is typically altered significantly upon binding of a molecule A to its target T. In contrast, the pH dependence of the dye $\partial F/\partial \text{pH}$ is intrinsic and should not be affected. Parts a and b of Figure 2 show that the normalized fluorescence time traces and radial distributions differ quantitatively and qualitatively when the binding state of the fluorescent biomolecule is changed. The fluorescence labeling of one binding partner provides the selectivity of measurements for specific binding reactions even in complex mixtures.

Quantification of Biomolecular Binding Interactions. To determine the binding affinity of the thrombin aptamer TBA15 to its target human-α-thrombin, we monitor the fluorescence of the labeled aptamer during photochemical microscale electrophoresis. To this end, an ATTO633 dye is attached to the 15nt aptamer. Two extra bases serve as a spacer. In titration experiments under constant buffer conditions, the thrombin concentration is varied from 19.5 μM to 595 pM, while the aptamer concentration is kept constant at 200 nM.

As shown in Figure 2c, a two-state binding curve is obtained when F_{norm} in steady state is plotted against the target concentration. In the limiting case of very low target concentrations, F_{norm} corresponds to the signal of the fully unbound state F_{norm}^A. At very high target concentrations, the limiting fluorescence represents the fully bound state F_{norm}^{AT}. In between, the fluorescence signals of the two states superpose linearly. This leads to a linear dependence of F_{norm} on the fraction of bound concentration with respect to all labeled concentrations $x = c^{AT}/(c^A + c^{AT})$:

$$F_{norm} = (1 - x)F_{norm}^A + xF_{norm}^{AT} \qquad (3)$$

Here, x is described by the quadratic solution of the equilibrium binding reaction equation derived from the law of mass action and can be fitted to the experimental binding curve. The dissociation constant K_D of the binding reaction is the only free parameter, as the total concentrations of the two binding partners are known throughout the experiment. The full fit equation is presented in the Experimental Section (eq 5). A detailed derivation can be found in the Supporting Information.

In Figure 3, we show the binding curves for two exemplary systems, the binding of thrombin to its aptamer and the hybridization of DNA. Here, we rescale the normalized fluorescence between the bound and unbound state so that the ordinate shows the fraction of bound molecules. For the aptamer–thrombin binding, we find a K_D of 1.04 ± 0.4 nM (Figure 2a, blue) using a constant aptamer concentration of 5 nM and thrombin titration from 2.5 μM to 38 pM. This result corresponds well to the K_D of 1.2 nM found by Ahmad et al.[28] The error bars in the binding curve indicate the standard deviation from data analysis at different distances from the laser focus. To further verify our findings, we measure the same binding curve by the well-established microscale thermophoresis (MST) method. The binding curve (Figure 3a, black) and
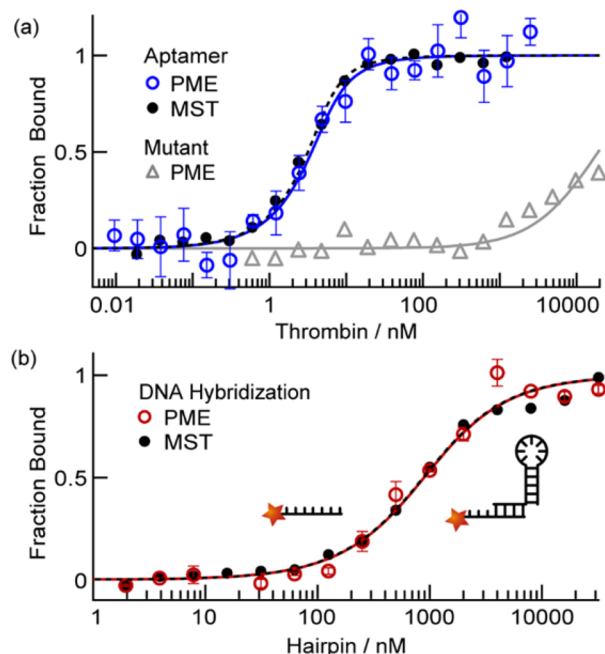
Figure 3. Biomolecule-binding quantification. Binding curves are fitted by the mass action law of the binding equilibrium (eq 5). (a) Thrombin−aptamer binding using an aptamer concentration of 5 nM and a mutant concentration of 200 nM. The PME binding curve yields a K_D of 1.04 ± 0.4 nM (blue) and matches the MST control experiment with K_D = 0.68 ± 0.11 nM (black). PME binding analysis of a dinucleotide mutant shows strongly reduced binding (gray). (b) Quantification of DNA hybridization using a constant ssDNA concentration of 500 nM. Binding curves from PME (red, K_D = 643 ± 28 nM) are accurately followed by the MST control (black, K_D = 632 ± 10 nM) and match calculations from the NUPACK package[27] (K_D = 640 nM).

the fitted K_D of 0.68 ± 0.11 nM are in good agreement with our results from PME. An MST experiment without added NBA shows a K_D of 0.8 ± 0.11 nM and ensures that the addition of NBA does not affect the binding significantly (Figure S2).

Moreover, we confirm the specificity of the aptamer−thrombin binding by measuring the binding curve for a dinucleotide mutant of TBA15 (Figures 2c and 3a, gray). We find a strongly reduced binding behavior in accordance with literature.[8]

To show the generality of the method and the precision in observing the mass action law, we also quantify the hybridization between a 24nt ssDNA and a hairpin (69nts) with eight complementary nucleotides in the toehold sequence. The concentration of the ssDNA is kept constant at 500 nM, while the hairpin concentration is varied between 32 μM and 2 nM. We find a K_D of 643 ± 28 nM using PME (Figure 3b, red). The result agrees very well with the MST control (Figure 3b, black), which yields a K_D of 632 ± 10 nM and with calculations by the NUPACK package,[27] which predicts a K_D of 640 nM.

We find a good agreement of our measurements with literature and MST control measurements. However, by inducing concentration changes of all reaction partners, we shift the binding equilibrium, given by the law of mass action. This induces an error in K_D fitting. In all experiments we keep the depletion and accumulation amplitudes small to minimize the error. For the presented binding curves, the deviation between observed and real K_D amounts to less than 3%,

significantly below the statistical error. The full calculation can be found in the Supporting Information.

Evaluation of the Binding Assay. To evaluate the quality of our binding assay, we follow the procedure proposed by Zhang et al.[29] They introduce a simple, dimensionless parameter, called the z-factor, which takes into account the dynamic range of the assay and data variation. Assays with z-factors larger than 0.5 are considered "excellent assays".[29] For the thrombin−aptamer binding curves we find z-factors of 0.9 (Figure 2c) and 0.47 (Figure 3a). The reduced z-factor for the binding curve in Figure 3a originates from the 40-fold lower aptamer concentration and the consequentially lower fluorescence intensities. However, the low concentration of 5 nM is required for the determination of K_D, as the fitting procedure becomes insensitive for $c_{Aptamer} \gg K_D$.[30] In addition, we find a satisfying z-factor of 0.78 for the quantification of DNA hybridization (Figure 3b).

Estimation of the Induced Electric Potential. We can use the steady-state fluorescence profile of a molecule with known electrophoretic mobility μ and diffusion coefficient D to estimate the photochemically induced electric field. To this end, we rearrange eq 2 and obtain

$$\phi(r) = \frac{D}{\mu}\left(1 - F_{norm}(r) + \frac{\partial F}{\partial pH}\Delta pH(r)\right) \tag{4}$$

The steady-state radial fluorescence distribution in the fully unbound state stems from transport of ssDNA. Single-stranded DNA is a well-studied biomolecule and literature provides values for μ and D (17 nt: $D = 160$ μm²/s, $\mu = -3.1 \times 10^{-8}$ m²/V/s; 24nt: $D = 133$ μm²/s, $\mu = -3.1 \times 10^{-8}$ m²/V/s).[31,32] We neglect the last term in eq 4 for the thrombin−aptamer experiments, as the used dye ATTO633 does not show a pH dependence (Figure S3).[33] However, for Cy5, which is used for the DNA hybridization experiments, it has to be taken into account. We find a pH dependence of fluorescence of 10% per pH unit (Figure S3).

Figure 4a shows the calculated potential distributions for all buffer conditions of the measured binding curves presented earlier, calculated by eq 4. For the aptamer binding curves in
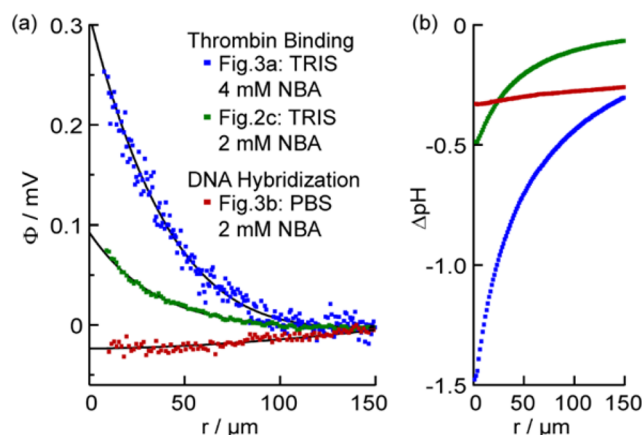

Figure 4. Radial distribution of pH and Φ for the three conditions, which correspond to the binding curves in Figures 2 and 3. (a) Induced electric potential calculated from the steady-state fluorescence distribution in the fully unbound state using eq 4. Solid lines are plotted to guide the eyes. (b) Radial pH distribution in steady state, measured by SNARF-4F fluorescence. TRIS-buffer (green, blue) offers only a reduced pH stability in comparison to PBS (red).

Figures 2c and 3a, we find maximum electric potentials of approximately 80 and 280 μV, respectively. Both experiments are performed in TRIS-based aptamer selection buffer at 500 μW laser power but at different NBA concentrations. As expected, the induced potential increases with increasing concentration of NBA.

The red curve corresponds to the DNA hybridization experiment. The pH dependence of the dye is included in the calculation. Interestingly, the amplitude and even the sign of the measured potential of −20 μV differs in comparison to the green curve. In both experiments NBA concentration and laser power are the same. However, the buffer conditions are different. This indicates the already discussed strong buffer dependence of electric field generation in PME. Only a shallow potential gradient is generated in the hybridization experiment. This emphasizes that a binding contrast can even be observed at extremely low field strengths.

Measurements of pH Profiles. NBA photolysis is always accompanied by a local pH change, since a proton is released by the photoreaction. For the binding measurements, we keep the photolysis rate and the pH change low to minimize the disturbance of the binding reaction. We optically monitor the pH in our samples using the ratiometric fluorescent dye SNARF-4F.

Figure 4b shows the radial pH distribution in steady state for all binding conditions. As expected, the pH change increases for larger NBA concentrations. In this respect, we find local pH changes of 1.2 and 0.5 units for the two thrombin experiments. For the DNA hybridization experiments we find a pH decrease of only 0.3 units (Figure 4b).

Interestingly, the shape of the pH gradient is strongly influenced by the buffer conditions. In PBS buffer, the pH shows only a shallow radial gradient. In contrast, a steep radial gradient builds up in the thrombin selection buffer, which is based on TRIS. A possible explanation are the pK_A's of TRIS (pK_A = 8.2) and phosphate (pK_A = 7.2). Only for the TRIS buffer, the pH locally decreases far below the effective buffering range and allows a large pH decrease.

In a simplified picture, this could also explain the different shapes of the electric potential in Figure 3a. Below the effective buffering range, the electric field is determined by the difference in diffusion speed of the two photoproducts NS$^-$ and H$^+$. Under buffering conditions, the effective diffusion speed of H$^+$ is dictated by the diffusion speed of the buffer molecules, which is much slower. Hence, the generated electric field in buffered solutions is typically smaller and can even be reversed.

In total, the results show that large shifts or steep gradients in pH are not required for a successful binding quantification. A balance between a sufficient signal-to-noise ratio, related to the photolysis rate, and the induced pH change has to be found.

■ DISCUSSION

We developed a method to induce size-selective microscale free-solution electrophoresis for the quantification of binding interactions. We drive the electric field by a local photochemical reaction followed by differential diffusion of the photoproducts. The electrophoresis of biomolecules is balanced by back-diffusion within tens of seconds, reaching a steady state which depends both on the electrophoretic mobility and the diffusion coefficient. This renders PME size selective even for highly charged, free draining polyelectrolytes, such as DNA. In contrast to macroscopic free solution electrophoresis, back-diffusion breaks the charge-friction balance without the use of drag tags[16] or sieving matrices.[17]

In our PME measurements, we only apply extremely low electric fields <2 V/m. This is 2−3 orders of magnitude lower than the fields applied in gel-, capillary-, or microelectrophoresis and prevents Joule heating. Moreover, our approach is all-optical and electrode-free. Thus, it circumvents electrode artifacts as aggregation, sticking to the surface, contamination, outgassing, and electrochemical effects.

The generation of electric fields by photochemistry is a complex electrokinetic process. The field is determined by the interplay of diffusion, electrophoresis and buffering reactions of all the ionic species in the solution. As NBA releases a proton upon photolysis, the concentration and electro-diffusive properties of buffer molecules, as well as the buffer reaction kinetics, play an important role. This can be seen in Figure 4 (red and green curves). At equal NBA concentration and laser power but under different buffer conditions, the strength and even the sign of the induced electric potential differ significantly.

For affinity quantification with PME, the existence of an electric field is required. Its magnitude and sign are irrelevant for the method as long as it remains constant for the experimental titration series. Conveniently, buffer conditions are typically constructed such that they remain constant under the titration of a binding partner.

We expect that a wide range of photoactive compounds may give rise to microscale electrophoresis, allowing one to tune the conditions to the biomolecular binding reaction at hand. As an example, photolysis of hexacyanoferrate(II) (Fe(CN)$_6^{4-}$) induces a reversed electric field in comparison to NBA under the same buffer conditions: DNA is attracted to the central laser spot, instead of being repulsed (Figure S4).

Binding analysis with PME is performed in solution and does not involve immobilization of a binding partner, which could introduce artifacts from the nearby surface. Approaches based on complex microfluidics[34] or specialized cells often involve a high final cost of the assay.[15] This bears the need to reuse expensive components with the risk of cross-contamination. In contrast, all-optical PME will allow the usage of disposable standard containers, such as multiwell plates for fast high-throughput screening. PME is a promising candidate for such applications, as it also requires only minute sample amounts (nL to μL) at low sample concentrations (nM). In our experiments, we use 1 μL sample volume per measurement but only probe about 2 nL. The low observation volume offers the possibility to further cut down the total sample consumption to 10 nL by using acoustic droplet dispensers, as already demonstrated for microscale thermophoresis.[35] The measuring protocol of PME is simple and similar to MST.[8] However, the underlying physical principles are markedly different and possibly more flexible. No temperature gradients are applied. Therefore, PME avoids thermal effects as thermal lensing and Marangoni flows.[35] Moreover, PME does not demand the tight geometrical definition in the direction of light propagation, which is needed in thermophoresis to avoid continuous heating and convection artifacts.[36]

Binding experiments in vivo are of considerable interest, as it is known, that kinetics is different in the crowded environment of a cell.[38−40] Recently, Reichl et al. succeeded in measuring thermophoresis inside living cells for the first time.[37] This approach is limited by the tight geometrical constraints and averaging artifacts introduced by the cell geometry. These

problems can be overcome by PME, which should open the future possibility to perform electrophoretic binding measurements inside cells. Photochemically induced fields are highly local and can in this way also circumvent the problem of the electrostatic insulation by the cell membrane.

PME does not suffer from thermal artifacts, but photolysis of NBA is always accompanied by a pH decrease as protons are released. We kept the pH changes small (0.3−1.5 pH units) to minimize the influence on the binding assay in order to ensure the applicability to biological systems. It should be noted that this influence can be tested by performing the experiments for constant K_D under a variation of the 375 nm laser power. In this regard, it should also be kept in mind that temperature changes, as applied in MST, are also often accompanied by pH changes. For example, the pK_A of TRIS is temperature dependent, and a temperature increase of 10 K leads to a pH shift of 0.3 units.[41] However, in principle, it should even be possible to avoid pH changes by PME altogether. To achieve this, a photoactive compound with pH neutral photoproducts must be found.

Instead of attempting to mitigate pH changes, we could in future also exploit them. Under strong photolysis and weak buffering, extreme pH gradients can be envisaged. Abbruzzetti et al. already used NBA to induce large, spatially homogeneous pH jumps for the observation of pH dependent unfolding of proteins.[42,43] In our system, the combination of steep pH gradients with electric fields should give rise to isoelectric focusing, triggered all-optically on the microscale in bulk water.

PME is an electrokinetic phenomenon. Local photolysis of a photoactive compound into two charged photoproducts always gives rise to an ionic strength gradient. This can induce another contribution to the transport equation, called chemiosmotic diffusiophoresis, which was first described by Prieve et al.[44] For our binding analysis we neglected diffusiophoresis, because the contribution is small and in first approximation size independent[45] at the used high ionic strengths and under strong buffering.

Still, especially at low ionic strength, diffusiophoretic transport should play a role in PME measurements. Experiments in simple electrolytes show that diffusiophoresis is governed by $\log(\nabla I)$, where I is the ionic strength.[46] The logarithmic scaling gives rise to interesting phenomena, such as controlled trapping and release of colloids by solute contrast[45,47] and long-range exclusion zone formation.[48] Progress in this direction with our approach requires a better theoretical understanding of the complex interactions between buffer reactions, diffusion, electro- and diffusiophoresis. A full theoretical treatment is nontrivial and requires very detailed experimental tests and a full description of the buffer dynamics under diffusion to determine all the parameters. This will be approached in a subsequent manuscript.

In summary, localized photolysis provides a versatile nonequilibrium system, which comprises pH and ionic strength gradients as well as electric fields. The coupling to physical transport is very likely to lead to new biological insights into cellular processes. For example, it has already been shown that pH-dependent selective transport and distribution of proteins inside living cells can play an important role in intracellular protein sorting and trapping.[49]

CONCLUSION

We present a method to rapidly generate microscale electric fields without electrodes in solution. We show how they can be used to measure the binding affinities of biomolecules in the nano- to micromolar regime in nanoliter volumes within minutes. The measurement protocol is simple, all-optical and can be applied to liquid volumes in various microscale geometries. The cross-coupling of photochemical reactions with physical transport suggests many future possibilities, including isoelectric focusing and the all-optical measurement of electrophoretic mobilities.

■ EXPERIMENTAL SECTION

Materials. Human-α-thrombin was purchased from CellSystems Biotechnologie Vertrieb GmbH (Troisdorf, Germany; Specific Activity: 2871 U/mg, MW = 36.7 Da). DNA oligonucleotides were synthesized by biomers GmbH, Germany. The sequences are as follows with mutations as small letters: thrombin aptamer TBA15 with two spacer bases: 5′-ATTO633TGGTTGGTGTGGTTGGT-3′, aptamer dinucleotide mutant: 5′-ATTO633TGGTTGtTGTGGTTt-GT-3′, hairpin: 5′-CGTCCCGTCCGTGGAGGAGAGTTTCGC-CTCCTCCACGGACGGGACGCTAATCGCTTTTTTTTCTACT-GTT-3′, ssDNA: 5′-Cy5-GCCATCGAAGTTTTTGCGATTAGG-3′,

Thrombin aptamer measurements were performed in its selection buffer (20 mM Tris−HCl pH 7.4, 150 mM NaCl, 5 mM KCl, 1 mM CaCl$_2$, 1 mM MgCl$_2$, 0.01% Tween20, 4% BSA, 2% Glycerol). DNA hybridization measurements were performed in 1× PBS with 250 mM added NaCl at pH 7.2. The caged proton 2-nitrobenzaldehyde (72780, Sigma-Aldrich, Taufkirchen, Germany) was added to samples at 2 mM (200 nM aptamer and DNA hybridization) or 4 mM (5 nM aptamer) concentration. To reduce photobleaching, a commercial oxygen scavenging system (MO-A001, Nanotemper technologies, Munich, Germany) was used for the 5 nM aptamer and the DNA hybridization measurements.

Serial Dilutions. For the binding curves, 2-fold serial dilutions with at least 15 steps were performed. Start concentrations were 19.5 μM thrombin (binding curves with constant aptamer and mutant concentrations of 200 nM), 2.5 μM thrombin (binding curves at 5 nM aptamer concentration), and 32 μM hairpin for the DNA hybridization curve with a constant labeled ssDNA concentration of 500 nM. All solutions were incubated for at least 30 min prior to experimentation to fully ensure that the binding equilibrium is reached. All PME measurements were performed at room temperature.

Imaging. For fluorescence imaging we used a Zeiss Axiotech Vario microscope with a 40× oil objective (Fluar, 40-fold, NA 1.3, Zeiss, Germany). The fluorescence signal was detected from above with an ORCA-Flash 4.0 Digital CMOS camera (Hamamatsu AG, Japan). For ATTO633 and Cy5 imaging fluorescence was excited with a 627 nm LED (LEDC28, Thorlabs). Fluorescence filters (Omega Optical Set XF110-2: XF1069 630AF50, XF2035 650DRLP, XF3076 695AF55) were purchased from Laser Components GmbH (Olching, Germany). For ratiometric pH imaging an Optosplit 2 (Cairn Research, Faversham, UK) was employed. Excitation was provided by a 470 nm LED (M470L2-C4, Thorlabs) and a ratiometric fluorescence filterset (F71-045: BrightLine HC 482/35, HCBS506, BrightLine HC 580/23, H606LP, Brightline XF 643/20) was purchased from AHF Analysentechnik AG (Tübingen, Germany). Rectangular Borosilicate glass capillaries (ID 0.5 × 0.05 × 50 mm^3, CMScientific, Silsden, UK) were used as transparent reaction containers for all measurements. To avoid drifting of the solution, capillaries were sealed with plasticine on both ends.

Photolysis. Localized photolysis was achieved by a TE-cooled 375 nm laser diode (20 mW, L375P020MLD and TCLDM9, Thorlabs, Germany). The laser light is coupled into a single mode fiber (P3-305A-FC, Thorlabs), collimated by an adjustable collimator (CFC-8X-A, Thorlabs), and focused by a lens (A240TM-A, Thorlabs) with a calculated conical divergence angle of approximately $\Theta = 0.10 \approx 6°$ to the center of the capillary. With fluorescence we observe a laser profile with 3 μm half width at half-maximum intensity. The laser ran in continuous mode and was switched on and off by a mechanical shutter system (SH05, Thorlabs, Germany). An optical chopper system (MC2000-EC, Thorlabs) was synchronized to the camera to

avoid detection of direct excitation by the 375 nm laser. Fluorescence images were taken, when the laser was blocked. The laser power was adjusted to 500 μW by a continuous neutral density filter wheel (NDM4/M, Thorlabs) and monitored by redirecting a fixed fraction of the beam to a powermeter (S120VC, Thorlabs).

Microscale Thermophoresis. All MST measurements were performed in standard treated capillaries (MO-K002, Nanotemper Technologies, Munich, Germany). Aptamer binding curves at 5 and 1 nM aptamer concentration were measured with a Monolith NT.115Pico (Nanotemper Technologies, Munich, Germany) at 22 °C and 40% MST Power, which corresponds to a maximal temperature change of approximately 10 K. The control measurements for the hairpin binding with 500 nM ssDNA were performed with the Monolith NT.015 (Nanotemper Technologies, Munich, Germany) using a laser power setting of 0.8 at a base temperature of 22 °C.

PME Image Analysis. For all measurements, a fluorescence background image without labeled molecules was subtracted. For the 200 nM aptamer (Figure 2) and the DNA hybridization (Figure 3b) assays the fluorescence was normalized against the initial fluorescence F_0. For the 5 nM aptamer binding assay (Figure 3a), fluorescence was normalized by the fluorescence 220 μm away from the laser spot to correct for photobleaching. F_{norm} is always averaged within an area with $\delta r = 5$ μm and a time interval of 25 s in steady state. For the binding curve in Figure 2, the fluorescence was evaluated at a radial area of $r + \delta r = 5 + 5$ μm. For the binding curves in Figure 3, the error bars represent the standard deviation from analyses at at least two different radii (5 nM aptamer: r = 20, 40, 60, 80, 200 μm; DNA hybridization r = 70, 90 μm). A derivation of the procedure can be found in the Supporting Information.

Binding Analysis. The normalized fluorescence after PME directly linearly reports on the fraction of bound molecules x (eq 3). The binding affinities were determined by fitting x to the quadratic solution of the binding reaction equilibrium, derived from the law of mass action:

$$x = \frac{c_{tot}^A - c_{tot}^T + K_D - \sqrt{(c_{tot}^A + c_{tot}^T + K_D)^2 - 4c_{tot}^A c_{tot}^T}}{2c_{tot}^T} \quad (5)$$

The total concentration of the labeled molecule c_{tot}^A and of the target c_{tot}^T were known, leaving K_D as a single fit parameter. Also here, a detailed derivation is presented in the Supporting Information.

Ratiometric pH Imaging. For pH imaging, we used the ratiometric dyes SNARF-4F (SNARF-4F 5-(and-6)-carboxylic acid, Invitrogen AG, Carlsbad, CA) or SNARF-1 (5-(and-6)-Carboxy SNARF-1, Invitrogen AG, Carlsbad, CA) at a concentration of 50 μM. We took fluorescence images at $\lambda_1 = 580$ nm and at $\lambda_2 = 640$ nm simultaneously using an Optosplit beam splitting device. After background subtraction, the fluorescence intensity ratio R = $F^{\lambda 1}/F^{\lambda 2}$ was calculated and converted into pH by a modified Henderson−Hasselbalch equation,[50] which is described in more detail in the Supporting Information:

$$pH = a + b \log\left(\frac{R - R_A}{R_B - R}\right) \quad (6)$$

R_A, R_B, a, and b were experimentally determined by fitting eq 6 to a ratio-to-pH calibration curve. To this end, we measured R for 12 samples with pH values between 2 and 10 at constant SNARF concentration. For the range between pH 2 and 8 we used a 0.1 M citrate buffer and for the range between pH 8 and pH 11 a 0.1 M carbonate buffer.[51] The calibration curves for SNARF-4F and SNARF 1 are presented in Figure S5. The resulting fit parameters are as as shown in Table 1.

Table 1. Fit Parameters for Ratio-to-pH conversion

	R_A	R_B	a	b
SNARF-1	1.31	0.07	6.65	−1.35
SNARF-4F	0.94	0.02	6.26	−1.06

Calculation of SNR and z-Factors. We followed the procedure proposed by Zhang et al.[29] to evaluate the assay quality. The signal-to-noise ratio is calculated by

$$SNR = \frac{|F_{norm}^A - F_{norm}^{AT}|}{\delta} \quad (7)$$

For the rescaled binding curves, the amplitude $|F_{norm}^A - F_{norm}^{AT}|$ equals 1. The mean error δ includes the standard deviation between N independent measurements in the bound and unbound state σ_{AT}, σ_A:

$$\delta = \frac{\sigma_A + \sigma_{AT}}{N} \quad (8)$$

A dimensionless measure for assay quality is the z-factor. It takes into account the data variability and the dynamic range of the assay and is given by

$$z = 1 - \frac{6\delta}{|F_{norm}^A - F_{norm}^{AT}|} \quad (9)$$

A z-factor above 0.5 is considered as an "excellent" assay for binding detection.[29]

The calculated signal-to-noise ratios (SNR) and z-values for our binding curves are listed in Table 2 and confirm the applicability of our assay

Table 2. Evaluation of the Assay Quality[29]

	thrombin-aptamer binding		DNA hybridization
	Figure 3a	Figure 2c	Figure 3b
SNR	11	61	27
z-factor	0.47	0.90	0.78

ASSOCIATED CONTENT

S Supporting Information

The Supporting Information is available free of charge on the ACS Publications website at DOI: 10.1021/jacs.6b01756.

Sketch of the experimental setup. Derivation: PME reports on the fraction of bound molecules. MST control: NBA does not influence the binding. pH dependence of the fluorescent dyes. Comparison of PME using NBA and hexacyanoferrate(II). SNARF calibration. Long time behavior: steady state and back-diffusion (PDF)

AUTHOR INFORMATION

Corresponding Author

*dieter.braun@lmu.de

Notes

The authors declare no competing financial interest.

ACKNOWLEDGMENTS

REFERENCES

(1) Ellington, A. D.; Szostak, J. W. *Nature* **1990**, *346*, 818.

(2) Xiao, Y.; Lubin, A. A.; Heeger, A. J.; Plaxco, K. W. *Angew. Chem.* **2005**, *117*, 5592.

(3) Wan, Y.; Kim, Y.; Li, N.; Cho, S. K.; Bachoo, R.; Ellington, A. D.; Iqbal, S. M. *Cancer Res.* **2010**, *70*, 9371.

(4) Ng, E. W. M.; Shima, D. T.; Calias, P.; Cunningham, E. T.; Guyer, D. R.; Adamis, A. P. *Nat. Rev. Drug Discovery* **2006**, *5*, 123.

(5) Hanlon, A. D.; Larkin, M. I.; Reddick, R. M. *Biophys. J.* **2010**, *98*, 297.

(6) Pierce, M. M.; Raman, C. S.; Nall, B. T. *Methods* **1999**, *19*, 213.

(7) Olmsted, I. R.; Hassanein, M.; Kussrow, A.; Hoeksema, M.; Li, M.; Massion, P. P.; Bornhop, D. J. *Anal. Chem.* **2014**, *86*, 7566.

(8) Baaske, P.; Wienken, C. J.; Reineck, P.; Duhr, S.; Braun, D. *Angew. Chem., Int. Ed.* **2010**, *49*, 2238.

(9) Hellman, L. M.; Fried, M. G. *Nat. Protoc.* **2007**, *2*, 1849.

(10) Foulds, G. J.; Etzkorn, F. A. *Nucleic Acids Res.* **1998**, *26*, 4304.

(11) Yang, P.; Mao, Y.; Lee, A. W.-M.; Kennedy, R. T. *Electrophoresis* **2009**, *30*, 457.

(12) Pan, Y.; Karns, K.; Herr, A. E. *Electrophoresis* **2014**, *35*, 2078.

(13) Musheev, M. U.; Filiptsev, Y.; Okhonin, V.; Krylov, S. N. *J. Am. Chem. Soc.* **2010**, *132*, 13639.

(14) Swinney, K.; Bornhop, D. J. *Electrophoresis* **2002**, *23*, 613.

(15) Castro, E. R.; Manz, A. *J. Chromatogr. A* **2015**, *1382*, 66.

(16) Heller, C.; Slater, G. W.; Mayer, P.; Dovichi, N.; Pinto, D.; Viovy, J.-L.; Drouin, G. *J. Chromatogr. A* **1998**, *806*, 113.

(17) Meagher, R. J.; Won, J. I.; McCormick, L. C.; Nedelcu, S.; Bertrand, M. M.; Bertram, J. L.; Drouin, G.; Barron, A. E.; Slater, G. W. *Electrophoresis* **2005**, *26*, 331.

(18) Bock, L. C.; Griffin, L. C.; Latham, J. A.; Vermaas, E. H.; Toole, J. J. *Nature* **1992**, *355*, 564.

(19) Macaya, R. F.; Schultze, P.; Smith, F. W.; Roe, J. A.; Feigon, J. *Proc. Natl. Acad. Sci. U. S. A.* **1993**, *90*, 3745.

(20) Tsiang, M.; Jain, A. K.; Dunn, K. E.; Rojas, M. E.; Leung, L. L. K.; Gibbs, C. S. *J. Biol. Chem.* **1995**, *270*, 16854.

(21) Endy, D. *Nature* **2005**, *438*, 449.

(22) Khalil, A. S.; Collins, J. J. *Nat. Rev. Genet.* **2010**, *11*, 367.

(23) Levskaya, A.; Chevalier, A. A.; Tabor, J. J.; Simpson, Z. B.; Lavery, L. A.; Levy, M.; Davidson, E. A.; Scouras, A.; Ellington, A. D.; Marcotte, E. M.; Voigt, C. A. *Nature* **2005**, *438*, 441.

(24) Tucker, R.; Katira, P.; Hess, H. *Nano Lett.* **2008**, *8*, 221.

(25) Emond, M.; Le Saux, T.; Allemand, J.-F.; Pelupessy, P.; Plasson, R.; Jullien, L. *Chem. - Eur. J.* **2012**, *18*, 14375.

(26) Chirieleison, S. M.; Allen, P. B.; Simpson, Z. B.; Ellington, A. D.; Chen, X. *Nat. Chem.* **2013**, *5*, 1000.

(27) Zadeh, J. N.; Steenberg, C. D.; Bois, J. S.; Wolfe, B. R.; Pierce, M. B.; Khan, A. R.; Dirks, R. M.; Pierce, N. A. *J. Comput. Chem.* **2011**, *32*, 170.

(28) Ahmad, K. M.; Oh, S. S.; Kim, S.; McClellen, F. M.; Xiao, Y.; Soh, H. T. *PLoS One* **2011**, *6*, e27051.

(29) Zhang, J.-H.; Chung, T. D. Y.; Oldenburg, K. R. *J. Biomol. Screening* **1999**, *4*, 67.

(30) Lippok, S.; Seidel, S. A. I.; Duhr, S.; Uhland, K.; Holthoff, H.-P.; Jenne, D.; Braun, D. *Anal. Chem.* **2012**, *84*, 3523.

(31) Stellwagen, N. C.; Gelfi, C.; Righetti, P. G. *Biopolymers* **1997**, *42*, 687.

(32) Stellwagen, E.; Stellwagen, N. C. *Biophys. J.* **2003**, *84*, 1855.

(33) ATTO-TEC. Product Information: ATTO633 https://www.atto-tec.com/ (accessed Feb 10, 2016).

(34) Duong, T. T.; Kim, G.; Ros, R.; Streek, M.; Schmid, F.; Brugger, J.; Anselmetti, D.; Ros, A. *Microelectron. Eng.* **2003**, *67−68*, 905.

(35) Seidel, S. A. I.; Markwardt, N. A.; Lanzmich, S. A.; Braun, D. *Angew. Chem., Int. Ed.* **2014**, *53*, 7948.

(36) Jerabek-Willemsen, M.; Wienken, C. J.; Braun, D.; Baaske, P.; Duhr, S. *Assay Drug Dev. Technol.* **2011**, *9*, 342.

(37) Reichl, M. R.; Braun, D. *J. Am. Chem. Soc.* **2014**, *136*, 15955.

(38) Schoen, I.; Krammer, H.; Braun, D. *Proc. Natl. Acad. Sci. U. S. A.* **2009**, *106*, 21649.

(39) Gnutt, D.; Gao, M.; Brylski, O.; Heyden, M.; Ebbinghaus, S. *Angew. Chem., Int. Ed.* **2015**, *54*, 2548.

(40) Ebbinghaus, S.; Dhar, A.; McDonald, J. D.; Gruebele, M. *Nat. Methods* **2010**, *7*, 319.

(41) Durst, R. A.; Staples, B. R. *Clin. Chem.* **1972**, *18*, 206.

(42) Abbruzzetti, S.; Sottini, S.; Viappiani, C.; Corrie, J. E. T. *Photochem. Photobiol. Sci.* **2006**, *5*, 621.

(43) Abbruzzetti, S.; Viappiani, C.; Small, J. R.; Libertini, L. J.; Small, E. W. *J. Am. Chem. Soc.* **2001**, *123*, 6649.

(44) Prieve, D. C.; Anderson, J. L.; Ebel, J. P.; Lowell, M. E. *J. Fluid Mech.* **1984**, *148*, 247.

(45) Shin, S.; Um, E.; Sabass, B.; Ault, J. T.; Rahimi, M.; Warren, P. B.; Stone, H. A. *Proc. Natl. Acad. Sci. U. S. A.* **2016**, *113*, 257.

(46) Abécassis, B.; Cottin-Bizonne, C.; Ybert, C.; Ajdari, A.; Bocquet, L. *Nat. Mater.* **2008**, *7*, 785.

(47) Palacci, J.; Cottin-Bizonne, C.; Ybert, C.; Bocquet, L. *Soft Matter* **2012**, *8*, 980.

(48) Florea, D.; Musa, S.; Huyghe, J. M. R.; Wyss, H. M. *Proc. Natl. Acad. Sci. U. S. A.* **2014**, *111*, 6554.

(49) Baskin, E. M.; Bukshpan, S.; Zilberstein, G. V. *Phys. Biol.* **2006**, *3*, 101.

(50) Whitaker, J. E.; Haugland, R. P.; Prendergast, F. G. *Anal. Biochem.* **1991**, *194*, 330.

(51) Dawson, R. M. C.; Elliott, D. C.; Elliott, W. H.; Jones, K. M. *Data for Biochemical Research*, 3rd ed.; Oxford University Press: Oxford, 1986.